

Global model of lower band and upper band chorus from multiple satellite observations

Nigel P. Meredith,¹ Richard B. Horne,¹ Angélica Sicard-Piet,² Daniel Boscher,² Keith H. Yearby,³ Wen Li,⁴ and Richard M. Thorne⁴

Received 30 May 2012; revised 9 August 2012; accepted 11 September 2012; published 20 October 2012.

[1] Gyroresonant wave particle interactions with whistler mode chorus play a fundamental role in the dynamics of the Earth's radiation belts and inner magnetosphere, affecting both the acceleration and loss of radiation belt electrons. Knowledge of the variability of chorus wave power as a function of both spatial location and geomagnetic activity, required for the computation of pitch angle and energy diffusion rates, is thus a critical input for global radiation belt models. Here we present a global model of lower band ($0.1f_{ce} < f < 0.5f_{ce}$) and upper band ($0.5f_{ce} < f < f_{ce}$) chorus, where f_{ce} is the local electron gyrofrequency, using data from five satellites, extending the coverage and improving the statistics of existing models. From the plasmopause out to $L^* = 10$ the chorus emissions are found to be largely substorm dependent with the largest intensities being seen during active conditions. Equatorial lower band chorus is strongest during active conditions with peak intensities of the order 2000 pT^2 in the region $4 < L^* < 9$ between 2300 and 1200 MLT. Equatorial upper band chorus is both weaker and less extensive with peak intensities of the order a few hundred pT^2 during active conditions between 2300 and 1100 MLT from $L^* = 3$ to $L^* = 7$. Moving away from the equator midlatitude chorus is strongest in the lower band during active conditions with peak intensities of the order 2000 pT^2 in the region $4 < L^* < 9$ but is restricted to the dayside between 0700 and 1400 MLT.

Citation: Meredith, N. P., R. B. Horne, A. Sicard-Piet, D. Boscher, K. H. Yearby, W. Li, and R. M. Thorne (2012), Global model of lower band and upper band chorus from multiple satellite observations, *J. Geophys. Res.*, *117*, A10225, doi:10.1029/2012JA017978.

1. Introduction

[2] Space weather is an increasingly important natural hazard as society becomes ever more heavily dependent on satellite technology for communications, navigation, defense and Earth observation. The impacts of space weather on satellite operations range from momentary interruptions of service to a total loss of capabilities when a satellite fails. For example, during the 2003 Halloween geomagnetic storms 47 satellites experienced anomalies while one satellite, the \$450 M Midori-2 environmental research satellite, was a complete loss [Webb and Allen, 2004]. A major cause

of radiation damage to satellites in Earth orbit is relativistic electrons ($E > 1 \text{ MeV}$). These so-called “killer” electrons cause deep dielectric charging, the subsequent discharge of which may lead to unwanted commands and/or damage to components [e.g., Wrenn, 1995].

[3] Relativistic electrons in the Earth's radiation belts are usually confined to two distinct regions. The inner radiation belt, which lies between 1.1 and 2 Earth radii (R_E) in the Earth's geomagnetic equatorial plane, is relatively stable. In sharp contrast, the outer radiation belt, which lies between 3 and 7 R_E , is highly dynamic. In this region the flux of relativistic electrons can change by several orders of magnitude on a variety of different timescales ranging from minutes to tens of days [e.g., Blake et al., 1992; Baker et al., 1994] resulting from the delicate interplay of various transport, acceleration and loss processes [Thorne, 2010]. These processes all tend to be enhanced during geomagnetic storms which are ultimately driven by activity on the Sun. Intriguingly, geomagnetic storms may increase (50%), decrease (20%) or leave the flux of relativistic electrons in the radiation belts essentially unchanged (30%) [Reeves et al., 2003], emphasizing the need to include both source and loss processes in radiation belt models.

[4] Gyroresonant wave particle interactions play a key role in radiation belt dynamics [e.g., Horne, 2002; Thorne

¹British Antarctic Survey, Natural Environment Research Council, Cambridge, UK.

²Office National d'Etudes et Recherches Aérospatiales, Toulouse, France.

³Department of Automatic Control and Systems Engineering, University of Sheffield, Sheffield, UK.

⁴Department of Atmospheric and Oceanic Sciences, University of California, Los Angeles, California, USA.

Corresponding author: N. P. Meredith, British Antarctic Survey, Natural Environment Research Council, Madingley Road, Cambridge CB3 0ET, UK. (nmer@bas.ac.uk)

et al., 2005a]. Such interactions break the first and second adiabatic invariants leading to heating and acceleration by absorption of the waves and pitch angle scattering and loss to the atmosphere. One particularly important plasma wave that plays a crucial role in radiation belt dynamics is whistler mode chorus.

[5] Whistler mode chorus is an intense electromagnetic emission typically observed in the frequency range from $0.1-0.8f_{ce}$ [Tsurutani and Smith, 1977; Koons and Roeder, 1990] with a gap at $0.5f_{ce}$ [Tsurutani and Smith, 1974] separating the emissions into so-called lower band ($0.1f_{ce} < f < 0.5f_{ce}$) and upper band ($0.5f_{ce} < f < f_{ce}$) chorus. Chorus is generated outside the plasmopause near the geomagnetic equator [LeDocq *et al.*, 1998; Lauben *et al.*, 2002; Santolik *et al.*, 2004, 2005] by cyclotron resonant interaction with supra-thermal electrons [Kato and Omura, 2007; Omura *et al.*, 2008; Li *et al.*, 2008, 2009a] injected into the inner magnetosphere during storms and substorms. Consequently, chorus is observed largely outside the plasmopause and is substorm-dependent with the largest amplitudes being seen during active conditions [Meredith *et al.*, 2001, 2003; Li *et al.*, 2009b, 2011].

[6] Chorus waves play a dual role in radiation belt dynamics contributing to both the acceleration and loss of relativistic electrons [Bortnik and Thorne, 2007]. For example, chorus waves are thought to be largely responsible for the generation of radiation belt electrons on a timescale of 1–2 days during the recovery phase of geoeffective storms [e.g., Horne *et al.*, 2005, 2006]. In contrast, storm-time chorus at high latitudes causes microburst precipitation and may lead to losses of radiation belt electrons on the timescale of the order of a day [Lorentzen *et al.*, 2001; O'Brien *et al.*, 2004; Thorne *et al.*, 2005b]. There is also growing and compelling evidence to suggest that whistler mode chorus is the dominant source of plasmaspheric hiss [Bortnik *et al.*, 2008a, 2009, 2011; Chen *et al.*, 2012a, 2012b, 2012c], which is itself responsible for the formation of the slot region between the inner and outer radiation belts [Lyons and Thorne, 1973; Meredith *et al.*, 2007, 2009] and the quiet time decay of energetic electrons in the outer radiation belt [Meredith *et al.*, 2006a; Summers *et al.*, 2007; Lam *et al.*, 2007]. At lower electron energies, pitch angle scattering by whistler mode chorus is largely responsible for both the diffuse aurora [Thorne *et al.*, 2010; Ni *et al.*, 2011a] and the pulsating aurora [Nishimura *et al.*, 2010].

[7] There are several dynamic global models of the radiation belts which are based on diffusion models [e.g., Varotsou *et al.*, 2005, 2008; Fok *et al.*, 2008; Subbotin *et al.*, 2010; Albert *et al.*, 2009]. They require diffusion rates that are proportional to the wave magnetic field intensity. Since wave intensities can vary significantly with spatial location and geomagnetic activity accurate modeling requires the development of global models of the wave magnetic field intensity for the various relevant wave modes using data from several satellites. Here we develop a new model of whistler mode chorus by combining data from five satellites equipped to study plasma waves in the inner magnetosphere. The coordinate system used to describe the new model is introduced in section 2. The satellites, associated instrumentation, and data analysis techniques used to develop the model are described in section 3. Methods used to distinguish between chorus and other wave modes are described

in section 4. The chorus wave database and statistical survey are described in section 5 followed by a discussion of the inter comparison of the satellite data in section 6. The global morphology of lower and upper band chorus as a function of geomagnetic activity is then presented in section 7. Finally the results are discussed and the conclusions presented in sections 8 and 9 respectively.

2. Magnetic Coordinates

[8] Global statistical models of the wave intensities have traditionally been computed as a function of McIlwain L , magnetic local time (MLT) and magnetic latitude (λ_m) [e.g., Meredith *et al.*, 2001, 2003; Li *et al.*, 2009b, 2011]. However, radiation belt models calculate the phase space density of the electrons as a function of energy, pitch angle, L^* and time. Here, L^* is related to the third adiabatic invariant, Φ , and is given by:

$$L^* = \frac{-2\pi k_0}{\Phi R_E} \quad (1)$$

where k_0 is the Earth's magnetic dipole moment. Physically, L^* is the radial distance in Earth radii to the equatorial points of the symmetric shell on which the particles would be found if all the non-dipolar components of the trapping magnetic field were adiabatically removed.

[9] Since the particle data and global radiation belt models are ordered by L^* we develop our new global models of the chorus wave intensities as a function of L^* , MLT and λ_m . For the database L^* and MLT are computed using the ONERA-DESP library V4.2 (D. Boscher *et al.*, ONERA-DESP library V4.2, 2008), using the IGRF field at the middle of the appropriate year and the Olson-Pfizer quiet time model [Olson and Pfizer, 1977]. There are several time dependent external magnetic field models that can be used to represent active conditions but large uncertainties still remain during very disturbed periods [e.g., McCollough *et al.*, 2008] and most require solar wind parameters, which are not fully available for the earlier missions (DE1 and CRRES) used here. For our study we need to select a model that does not depend on solar wind parameters such as Mead-Fairfield 1975, Olson-Pfizer quiet 1977 and the Tsyganenko 1987 and 1989 models. We choose the Olson-Pfizer quiet time model here because it has been shown to be a good average external magnetic field model when compared to measurements [Friedel *et al.*, 2005] and has recently been adopted by the Panel for Radiation Belt Environment Modeling for improving space radiation models. Since the software is designed for particles and we are applying it to waves we assume a local pitch angle of 90° in the calculation of L^* . The magnetic latitude is calculated using a simple dipole magnetic latitude.

[10] To aid comparison with previous models we note that there is no simple transformation from L^* to L . However, as a general rule of thumb, at any given location the difference between L^* and L depends mostly on L^* and increases with increasing L^* . At low L^* the difference is relatively small with $L^* = 2$ mapping to L values in the range 2.05 to 2.10. At intermediate values of L^* , $L^* = 5$ maps to L values in the range 5.3 to 5.6. The difference is largest at large L^* with,

for example, $L^* = 8$ typically mapping to L values in the range 8.5 to 9.0.

3. Instrumentation and Data Analysis

[11] The instrumentation and data analysis techniques used in the development of the global model of whistler mode chorus from each of the five satellites are briefly described in sections 3.1–3.5. The data coverage provided by the relevant instrumentation on the five satellite missions is described in section 3.6.

3.1. Dynamics Explorer 1

[12] The NASA Dynamics Explorer 1 (DE1) spacecraft was launched on 3 August 1981 into a high altitude elliptical polar orbit with a perigee of 568 km, an apogee of 23,289 km and an inclination of 89.9°. The Plasma Wave Instrument (PWI) [Shawhan *et al.*, 1981] measured two components of the electric field and one component of the magnetic field in the frequency range between 1.78 Hz and 410 kHz. The full data set is available from September 1981 to June 1984, after which measurements above 100 Hz ceased due to a hardware failure. The SFC Step Frequency Correlator, composed of two Step Frequency Receivers, provided the spectral density of the electric and magnetic field coming from 128 frequency channels, logarithmically spaced between 105 Hz and 410 kHz. The temporal resolution of the SFR was 32 s: one measurement was performed each second for 4 frequencies and 32 seconds were needed for full frequency coverage. Since DE1 measures one component of the wave magnetic field in the spin plane, on average, over many rotations, the other spin plane component should have a similar intensity, and we estimate the total intensity in the spin plane by multiplying the single component by a factor of two. The power parallel to the spin axis, which is normal to the orbital plane, is not measured. The ambient magnetic field, used to calculate the local electron gyrofrequency, was provided by the magnetic field instrument (MAG) [Farthing *et al.*, 1981].

[13] To aid our analysis of the data, we first put the DE1 data into ISTP Common Data Format files (CDF) (http://spdf.gsfc.nasa.gov/sp_use_of_cdf.html). These files contain all the information necessary to construct the wave data base (electric and magnetic field of the waves, position of the spacecraft, electron cyclotron frequency measured by the spacecraft, L^* , local and equatorial magnetic field magnitude calculated with the ONERA library). Most of these parameters have a flag in the CDF files to state whether the data is good or not. Thus, the data were filtered, and only good data were used to develop the wave data base. Any remaining periods of corrupt data and sporadic bad points (“spikes”) were then removed from the data. Finally, all measurements outside the magnetosphere, which are outside the scope of this study, were removed using a magnetopause model [Shue *et al.*, 1998].

3.2. CRRES

[14] The Combined Release and Radiation Effects Satellite (CRRES), a joint NASA/Department of Defense (DOD) mission, was launched on 25 July 1990 into a highly elliptical geosynchronous transfer orbit, with a perigee of 350 km, an apogee of 33,584 km and an inclination of 18.1°.

The Plasma Wave Experiment (PWE) [Anderson *et al.*, 1992] provided measurements of wave electric fields from 100 Hz to 400 kHz in the spin plane, using a 100 m tip to tip long wire antenna, with a dynamic range covering a factor of at least 10^5 in amplitude. The sweep frequency receiver covered the frequency range from 100 Hz to 400 kHz in four bands with 32 logarithmically spaced steps per band. Band 1 (100 to 810 Hz) was sampled at one step per second with a complete cycle time of 32.768 s. Band 2 (810 Hz to 6.4 kHz) was sampled at two steps per second with a complete cycle time of 16.384 s. Band 3 (6.4 kHz to 51.7 kHz) and band 4 (51.7 kHz to 400 kHz) were each sampled four times per second, with a complete cycling time of 8.192 s. The wave electric field data consists of one component in the spin plane and we estimate the total power in the spin plane by multiplying the single component of the power by a factor of two, as in previous work. The power parallel to the spin axis, which lies in the ecliptic plane and points 12° ahead of the Sun in celestial coordinates, is not measured. The ambient magnetic field, used to calculate the characteristic frequencies, was provided by the fluxgate magnetometer instrument [Singer *et al.*, 1992]. The data set runs from 20 August 1990 until the satellite failed on 11 October 1991.

[15] The CRRES PWE data were initially corrected for the instrumental background response and smoothed using a running 3 minute average to take out the beating effects due to differences in the sampling and spin rate. Spurious data points, data spikes and periods of instrumental downtime were flagged and ignored in the subsequent statistical analyses. Twelve orbits, during which non-traditional configurations were deployed for testing purpose, were also excluded from the analyses. Reliable measurements of the wave magnetic field at VLF frequencies are not available from CRRES. Therefore, the wave electric field spectral intensities, S_E , were converted to magnetic field spectral intensities, S_B , using the expression:

$$S_B = \frac{1}{c^2} \left(1 + \frac{f_{pe}^2}{f(f_{ce} - f)} \right) S_E \quad (2)$$

derived from Maxwell’s third equation and using the cold plasma dispersion relation for parallel-propagating whistler mode waves. Here c is the speed of light, f is the wave frequency, f_{ce} is the electron gyrofrequency, and f_{pe} is the electron plasma frequency determined from the plasma wave data as described in Meredith *et al.* [2002]. Briefly, in the plasma-sphere f_{pe} is determined from emissions at the upper hybrid frequency, f_{uhr} . Further out, in the trough region, f_{uhr} is usually not well defined and the electron plasma frequency is estimated from the lower frequency limit of the electromagnetic continuum radiation, which is taken to be a plasma wave cutoff at the plasma frequency [Gurnett and Shaw, 1973]. The wave magnetic field intensities for lower band and upper band chorus, together with the corresponding number of samples, were subsequently rebinned as a function of half orbit (inbound and outbound) and L^* in steps of 0.1 L^* . The data were recorded together with the Universal Time (UT), MLT, and λ_m at the same resolution.

3.3. Cluster 1

[16] Cluster 1, one of the four spacecraft of the ESA Cluster mission, was launched on 9 August 2000 and

initially operated in a highly elliptical polar orbit with a perigee of 17,200 km, an apogee of 120,500 km and an inclination of 90.7° . The Spatiotemporal Analysis of Field Fluctuations (STAFF) experiment [Cornilleau-Wehrin *et al.*, 1997, 2003] consists of a three-axis search coil magnetometer to measure the wave magnetic field, a waveform unit and a Spectrum Analyzer. The Spectrum Analyzer combines the three magnetic components with the two electric field components measured by the Electric Fields and Waves (EFW) experiment [Gustafsson *et al.*, 1997] to compute the 25 auto and cross correlation coefficients of the spectral matrix at 27 frequencies distributed logarithmically in the range 8 Hz to 4 kHz. From the matrix we use the sum of the magnetic power spectral densities in three orthogonal directions. The WHISPER instrument [D  cr  au *et al.*, 1993, 1997] consists of a receiver, a transmitter and a Spectrum Analyzer, completed by the sensors of EFW and functions of the Digital Wave Processing Experiment. The WHISPER instrument provides measurements of the total electron density of the plasma, via relaxation sounder, and one component of wave electric field in the spin plane at 480 frequencies distributed logarithmically in the frequency range 2–80 kHz. The total power in the spin plane is then obtained by multiplying the single component by a factor of 2. The ambient magnetic field, used to calculate the electron gyrofrequency, is provided by the fluxgate magnetometer (FGM) [Balogh *et al.*, 2001]. For this study we used the data from Cluster 1 from 1 January 2001 to 31 December 2010. We assume that the three other spacecraft will not give more information, taking into account the similarity of the orbits.

[17] The wave electric field spectral intensities measured by WHISPER were initially converted to magnetic field spectral intensities using the cold plasma dispersion relation for parallel propagating waves described above. We then put the Cluster 1 data from the two instruments into the ISTP Common Data Format files (CDF). This resulted in a full wave magnetic field spectrum from 8 Hz to 80 kHz comprising 497 frequency channels with a transition between the two instruments at about 3.57 kHz. Periods of corrupt data and sporadic bad points (“spikes”) were excluded from the analysis together with measurements outside the magnetosphere as determined by a magnetopause model [Shue *et al.*, 1998].

3.4. Double Star TC1

[18] Double Star TC1, a joint China National Space Administration (CNSA)/ESA mission, was launched on 29 December 2003 into a highly elliptical equatorial orbit with a perigee of 562 km, an apogee of 78,970 km and an inclination of 28.2° . The STAFF experiment [Cornilleau-Wehrin *et al.*, 2005] on TC-1 consisted of a search coil antenna, three pre-amplifiers, a magnetic waveform unit, and power supply provided by CETP, and a Digital Wave Processor (DWP) provided by the University of Sheffield. The DWP computed the spectral matrix (3 power spectra plus the cross phase between each component) at 27 frequencies between 10 Hz and 4 kHz with a 1 s time resolution. Unfortunately the STAFF antenna boom failed to deploy, which meant interference from the spacecraft subsystems was very high. As a consequence of this, the DWP data were subsequently analyzed on the ground to minimize the

interference resulting from the non deployment of the antenna boom. Spectra acquired when large interference spikes occurred were rejected and the signals from two axes of the antenna were combined to synthesize a measurement in a direction where the continuous interference was least. The optimum direction has an inclination of between 11 and 17° from the spin plane depending on frequency, so the antenna is mostly sensitive to spin plane wave power. The measurements were averaged over approximately one spin period (4 s) and the total wave power spectral density in the spin plane was estimated by multiplying by a factor of 2. For this study we use the ground-processed wave data which cover the period from 5 January 2004 to 31 December 2004. The ambient magnetic field, used to calculate the characteristic frequencies, was provided by the magnetic field investigation [Carr *et al.*, 2005].

[19] The ambient magnetic field, used to determine the electron gyrofrequency, was determined from the fluxgate magnetometer at 4 s time resolution [Carr *et al.*, 2005], and the position in GSE coordinates was provided at a 1 minute time resolution from the European Payload Operations Service (EPOS) catalogue. The ambient magnetic field and spacecraft position were subsequently computed for the time of each STAFF measurement by linear interpolation. The wave magnetic field intensities for lower band and upper band chorus, together with the corresponding number of samples, were then rebinned as a function of half orbit (inbound and outbound) and L^* in steps of $0.1 L^*$. The data were recorded together with the Universal Time (UT), MLT, and λ_m at the same resolution. Data outside the magnetosphere were excluded from the analysis.

3.5. THEMIS A, D, E

[20] The five spacecraft of the NASA THEMIS (Time History of Events and Macroscale Interactions during Substorms) mission were launched on 17 February 2007 into near-equatorial orbits with apogees above $10 R_E$ and perigees below $2 R_E$ [Angelopoulos, 2008]. The three inner probes, THEMIS A, D, and E, sample whistler mode waves in the inner magnetosphere from 5 to $10 R_E$. The wave data used in this study were provided by the Search Coil Magnetometer (SCM) [Le Contel *et al.*, 2008; Roux *et al.*, 2008], which measures magnetic field fluctuations in the frequency range from 0.1 Hz to 4 kHz. The high resolution (fff) data used here consists of measurements of one component of the magnetic wave spectral density in the spacecraft spin plane, with a frequency resolution with 32 or 64 frequency bands logarithmically spaced over 4–4000 Hz [Cully *et al.*, 2008a]. This high resolution data was obtained by averaging spectra over 1 or 0.5 sec and recorded with a cadence of 8 s. The total wave power spectral density in the spin plane was then estimated by multiplying by a factor of 2. The high resolution wave power spectra data have been available since 1 May 2010 during the fast survey, with approximately 12 hours coverage per day. The ambient magnetic field used to calculate the electron gyrofrequency was provided by the Fluxgate Magnetometer (FGM) [Auster *et al.*, 2008].

[21] For this study, fff magnetic wave spectra data collected between 1 May 2010 and 1 October 2011 on THEMIS A, D, and E were used to investigate the global distribution of whistler mode chorus wave intensities. Waves observed

Table 1. Satellite Initial Orbits and Instrumentation

Satellite	Perigee (km)	Apogee (km)	Inc. (deg)	Instrument	Frequency Range
DE1	568	23,289	89.9	PWI	1.78 Hz to 410 kHz
CRRES	350	33,584	18.1	PWE	100 Hz to 400 kHz
Cluster 1	17,200	120,500	90.7	STAFF	8 Hz to 4 kHz
Cluster 1	17,200	120,500	90.7	WHISPER	2 kHz to 80 kHz
TC1	562	78,970	28.2	STAFF	8 Hz to 4 kHz
THEMIS	470	87,330	16.0	SCM	0.1 Hz to 4 kHz

inside the plasmasphere or outside the magnetopause were excluded following the method by *Li et al.* [2010a].

3.6. Data Coverage

[22] The satellite initial orbits together with the relevant instrumentation, and associated frequency ranges are tabulated for reference in Table 1. The data coverage of the missions used in the creation of the chorus model is plotted in Figure 1, together with a trace of the sunspot number, to show the coverage of the various satellites with respect to the phase of the solar cycle, and, for reference, traces of the daily averaged *AE* and *Dst* indices, which are measures of substorm and storm activity respectively. For this study we used approximately 3 years of data from DE1, 15 months of data from CRRES, 1 year of data from Double Star TC1, 10 years of data from Cluster 1 and 17 months of data from THEMIS. In terms of the phase of the solar cycle, the CRRES data were collected during the maximum of solar cycle 22, the DE1 and Double Star TC1 data were collected during the declining phase of solar cycles 21 and 23 respectively, the THEMIS data were recorded during the

ascending phase of solar cycle 24 and the Cluster data cover an entire solar cycle. All the different phases of the solar cycle are thus covered in our study.

4. Identification of the Wave Mode

[23] In the inner magnetosphere, plasmaspheric hiss and lightning generated whistlers, which are typically observed in the frequency ranges $100 \text{ Hz} < f < 2 \text{ kHz}$ and $2 \text{ kHz} < f < 5 \text{ kHz}$ respectively [*Meredith et al.*, 2006b], can overlap in frequency with whistler mode chorus which is typically observed in the frequency range $0.1f_{ce} < f < 0.8f_{ce}$ [*Tsurutani and Smith*, 1977; *Koons and Roeder*, 1990]. These wave emissions cannot, therefore, be clearly identified based on frequency alone. However, whistler mode chorus waves are largely observed outside the plasmopause [*Burtis and Helliwell*, 1976; *Tsurutani and Smith*, 1974, 1977]. In contrast, plasmaspheric hiss is characteristically confined to the higher density regions associated with the plasmasphere [*Dunckel and Helliwell*, 1969; *Russell et al.*, 1969; *Thorne et al.*, 1973] and plasmaspheric plumes [*Chan and Holzer*, 1976; *Cornilleau-Wehrin et al.*, 1978; *Parrot and Lefevvre*, 1986; *Summers et al.*, 2008] and lightning generated whistlers are largely confined to the plasmasphere [*Carpenter et al.*, 1968, 1969; *Platino et al.*, 2005]. Establishment of the spacecraft environment can therefore be used to discriminate between these plasmaspheric and trough emissions.

[24] Electrostatic waves in the frequency band $f_{ce} < f < 2f_{ce}$, which contain contributions from both electron cyclotron harmonic waves and thermal noise, tend to be excluded from the high density region inside the plasmopause. For CRRES, where electric field measurements are available in

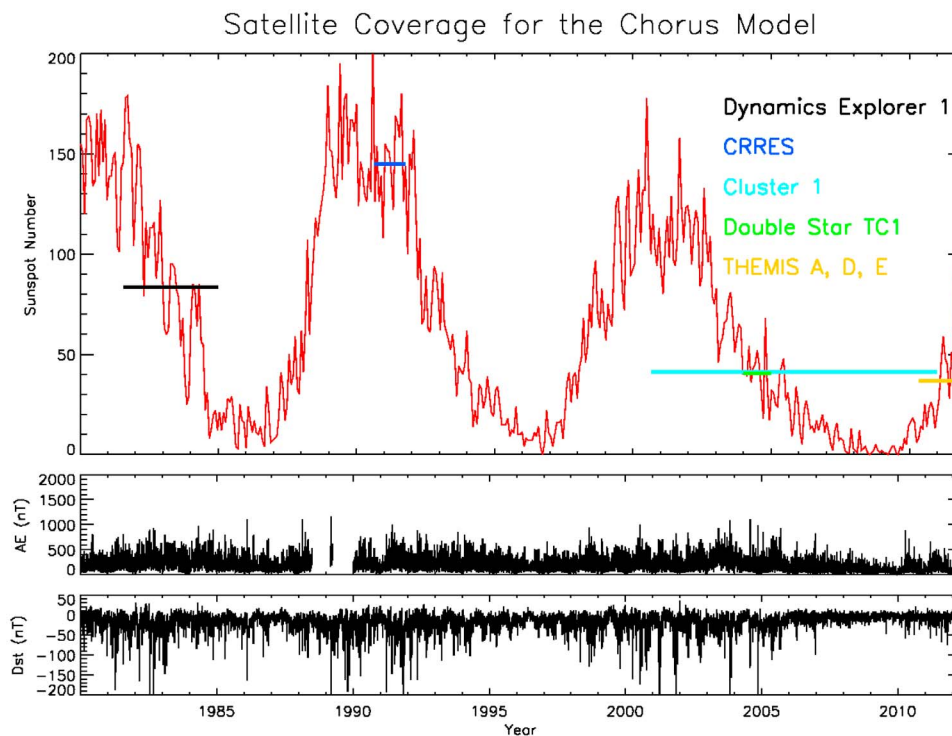


Figure 1. Satellite coverage for the chorus model together with traces of (top) the sunspot number, (middle) the daily averaged *AE* index, and (bottom) the 1 daily averaged *Dst* index.

Table 2. Format of the Wave Databases

Parameter	Bins
L^*	90 linear steps from $L^* = 1$ to $L^* = 10$
MLT	24 linear steps from 0 MLT to 24 MLT
λ_m	60 linear steps from -90° to 90°
Activity	10 activity levels as monitored by AE
Location	2 classes, inside or outside the plasmopause

the frequency range $f_{ce} < f < 2f_{ce}$, a given location was defined to be inside or outside the plasmopause when the wave amplitude in the frequency range $f_{ce} < f < 2f_{ce}$ was less than or greater than $5 \times 10^{-4} \text{ mV m}^{-1}$ respectively [Meredith et al., 2004].

[25] For THEMIS the wave emissions are categorized into either inside or outside the plasmopause following the method of Li et al. [2010a]. Specifically, the plasmopause is located at the position where the total electron density, inferred from measurements of the spacecraft potential and the electron thermal speed, is equal to N_c where $N_c = 50 \text{ cm}^{-3}$ for $L^* > 4.4$ and $N_c = 10(6.6/L^*)^4$ for $L^* < 4.4$.

[26] We were unable to devise a method of uniquely determining the position with respect to the plasmopause for DE1 and Cluster 1 using ECH waves, and Double Star TC1 made no measurements of ECH waves. For these satellites we revert to a model, and define a given location to be inside or outside the plasmopause when the L value of the observation is less than or greater than L_p where $L_p = 5.6 - 0.46 Kp^*$, Kp^* being the maximum value of the Kp index in the previous 24 hours [Carpenter and Anderson, 1992].

5. Chorus Wave Database and Statistical Survey

[27] Previous studies have shown that whistler mode chorus waves are observed primarily outside the plasmopause and the observed intensities depend on spatial location and substorm-activity, as monitored by the AE index [e.g., Tsurutani and Smith, 1974, 1977; Meredith et al., 2001, 2003; Li et al., 2009b, 2011]. Therefore, for each satellite the average wave intensities for lower band and upper band chorus, together with the corresponding number of samples, were binned as a function of L^* , MLT, λ_m , geomagnetic activity as monitored by the AE index, and location with respect to the plasmopause as detailed in Table 2.

[28] We subsequently combined the data from each of the satellites, weighting the data obtained from each individual satellite by the corresponding number of samples, to produce a combined chorus wave database as a function of L^* , MLT, λ_m , geomagnetic activity, and location with respect to the plasmopause.

[29] For the statistical survey presented here we split geomagnetic activity into three intervals which we define as quiet when $AE < 100 \text{ nT}$, moderate when $100 < AE < 300 \text{ nT}$, and active when $AE > 300 \text{ nT}$.

6. Intercomparison of the Satellite Data

[30] The instrumentation is different on each of the five satellites and no inter-calibration between missions is possible since the satellites operated at different times and in different environments. However, each instrument has been

calibrated by the respective instrument teams, and we rely on these calibrations here.

[31] Differences in sensitivity between the instruments can affect the average intensities but are limited to very low intensity levels when the spectral intensity is below the threshold for detection in one or more of the instruments. The effect is negligible when the wave power is well above the threshold for detection for all of the instruments, which roughly equates to wave power above 1 pT^2 . Since chorus wave power below 1 pT^2 is insignificant and has an insignificant affect on diffusion rates our model captures all of the important chorus wave power.

[32] We calculate the lower and upper band chorus wave intensities at any given time for any given instrument by integrating the wave spectral intensity over the frequency ranges $0.1f_{ce} < f < 0.5f_{ce}$ and $0.5f_{ce} < f < f_{ce}$ respectively. When all or part of a given frequency band lies outside the frequency range of a given instrument the data are discarded. When the frequency band of interest lies within the frequency range of the detector there are a number of frequency steps inside the band ranging from 9 to more than 20 for lower band chorus and 4 to more than 10 for upper band chorus depending on instrument. The frequency bands are thus well sampled and, for any given instrument, the integrated intensity should provide a good measure of the lower and upper band chorus wave power.

[33] The time resolution of the data sets used in this study ranges from 1 s to 32 s, which, for any given orbit, results in many samples in a given $0.1 L^*$ bin. However, the time resolution is not high enough to resolve the very large amplitude chorus waves which have been observed recently by several spacecraft [e.g., Cattell et al., 2008; Cully et al., 2008b]. These waves typically last for few tenths of a second and do not appear as very large amplitudes in the time averages of the wave data used in this study.

[34] Our database uses data from five satellites and six different instruments, all providing slightly different measurements of the wave magnetic field. The STAFF instrument on Cluster 1 is the most comprehensive providing three orthogonal components of the wave magnetic field, and we determine the total power by summing the power from these three components. For the other instruments we estimate the total power in the spin plane, noting that this treatment may underestimate the total power by up to a factor of two for a given whistler mode wave, depending on the orientation of the spin plane with respect to the ambient magnetic field.

[35] To compare the satellite observations we first investigate the behavior of the average lower band chorus intensities outside the plasmopause in the equatorial region ($-15^\circ < \lambda_m < 15^\circ$) as a function of spatial location and geomagnetic activity. Figure 2 shows the average wave intensities of lower band chorus outside the plasmasphere in the equatorial region as a function of L^* , MLT and geomagnetic activity for each of the five satellites. From top to bottom the panels show the results from DE1, CRRES, Cluster 1, Double Star TC1 and THEMIS as a function of L^* and MLT for, from left to right, quiet, moderate and active conditions respectively. Each plot extends linearly out to $L^* = 10$ with noon at the top and dawn to the right.

[36] The data coverage provided by all five satellites extends from the plasmopause out to $L^* = 10$. Inside $L^* = 5$, which includes the heart of the outer radiation belt, the

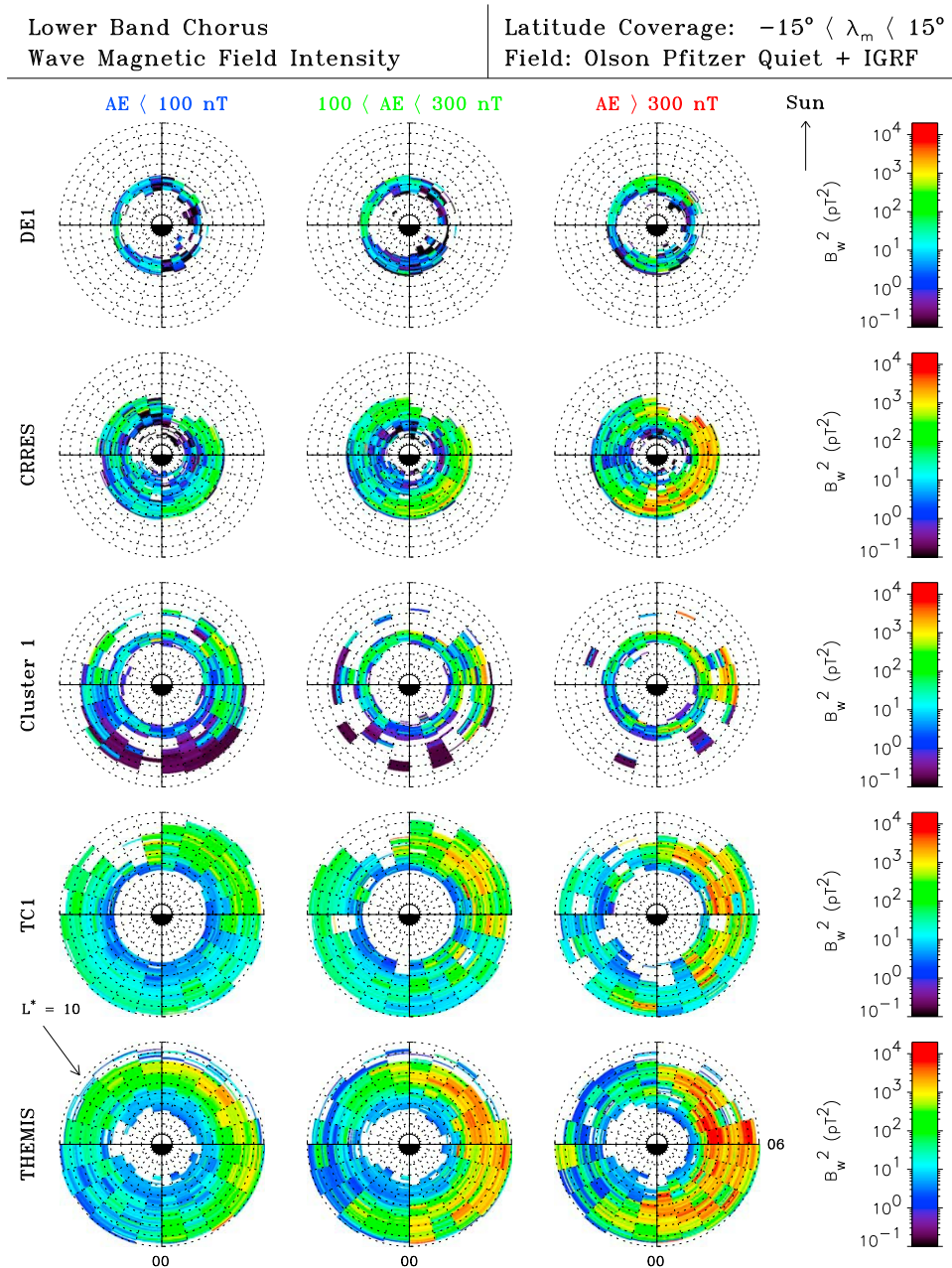


Figure 2. Equatorial wave intensity of lower band chorus as a function of L^* , MLT and geomagnetic activity for each of the five satellites.

equatorial coverage is largely provided by DE1, CRRES, Cluster 1 and THEMIS. Further out, in the region $5 < L^* < 6$, the data comes mostly from CRRES, THEMIS and Double Star TC1, and beyond $L^* = 6$ the equatorial coverage is largely provided by THEMIS and Double Star TC1. In particular, the gap in the coverage in the region $4 < L^* < 6$ for 0800–1200 MLT in global wave models derived from CRRES data [e.g., Meredith *et al.*, 2001, 2003] is filled in, primarily with data from Double Star TC1 and THEMIS. The largest intensities, of the order 2000 pT^2 , are seen during active conditions on the dawn-side.

[37] Figure 3 shows a comparison of the average intensity of lower band chorus observed within $\pm 9^\circ$ of the magnetic equator during active conditions measured by each of the

satellites as a function of MLT for a selection of L^* values for, from bottom to top, $L^* = 5.5 \pm 0.3$, 6.5 ± 0.3 and 7.5 ± 0.3 respectively. In each case the data have been smoothed by performing a running mean over 3 hours of MLT. At $L^* = 7.5$ (Figure 3, top) there is generally good agreement, largely to within a factor of 3 or so, between the THEMIS and Double Star TC1 data despite the average intensities varying by almost two orders of magnitude with MLT. Moving in, at $L^* = 6.5$ (Figure 3, middle) there is again good agreement, largely to within a factor of 3 or so between the THEMIS and Double Star TC1 data between 0200 and 0800 MLT. The two Cluster 1 measurements also show good agreement with the THEMIS and Double Star TC1 data at 0500 and 0600 MLT. From 1000 to 1300 MLT

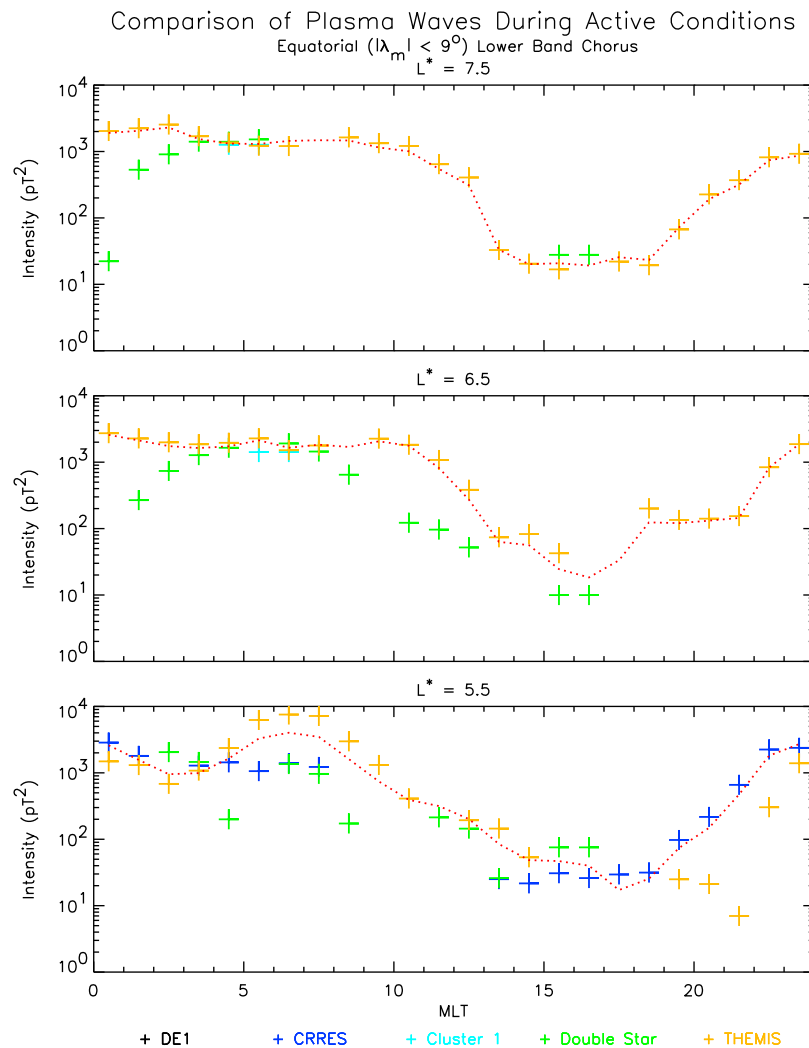


Figure 3. Average lower band chorus intensities within $\pm 9^\circ$ of the magnetic equator from each of the five spacecraft as a function of MLT at, from bottom to top, $L^* = 5.5$, 6.5 and 7.5 , respectively.

THEMIS measures consistently higher average intensities than Double Star TC1. At $L^* = 5.5$ (Figure 3, bottom) there is more scatter but generally good agreement between the CRRES, THEMIS and Double Star TC1 values between 0200 and 1700 MLT. From 1900 to 2200 MLT CRRES generally measures larger intensities than THEMIS.

7. Global Morphology of Lower and Upper Band Chorus

7.1. MLT Distribution

7.1.1. Equatorial Region ($|\lambda_m| < 15^\circ$)

[38] The average equatorial ($|\lambda_m| < 15^\circ$) lower band chorus intensities are shown as a function of L^* , MLT and geomagnetic activity in Figure 4 (bottom). The average intensities are shown in the large panels and the corresponding sampling distributions are shown in the small panels. The results are shown for, from left to right quiet, moderate and active conditions. During quiet conditions the lower band chorus intensities are generally weak and less than 100 pT^2 inside $L^* = 6$. Further out the intensities remain weak and below 100 pT^2 in the region from 1600 to 0400 MLT.

However, larger intensities in the range of several hundred to 1000 pT^2 are observed in the region $7 < L^* < 9$ from 0400 to 1600 MLT even though the AE index is below 100 nT. The average lower band chorus intensities increase during moderate conditions with the largest intensities, of the order 1000 pT^2 , being seen primarily in the region $6 < L^* < 9$ in the pre-noon sector from 0500 to 1100 MLT. The lower band chorus is strongest and covers the largest region of geospace during active conditions, with peak intensities of the order 2000 pT^2 predominantly in the region $4 < L^* < 9$ from 2300 to 1200 MLT.

[39] The average equatorial upper band chorus intensities are shown as a function of L^* , MLT and geomagnetic activity in Figure 4 (top). The equatorial upper band chorus is generally weaker and less extensive than the corresponding lower band chorus. During quiet conditions weak intensities in the range $10\text{--}40 \text{ pT}^2$ are seen in the region $5 < L^* < 7$ from 0100 to 1500 MLT. Elsewhere, the intensities fall below 10 pT^2 . Larger intensities, up to about 100 pT^2 are seen during moderate conditions in the region $4 < L^* < 7$ from 2300 to 0100 MLT. During active conditions intensities can exceed 100 pT^2 in the region $3 < L^* < 7$ from 2300 to

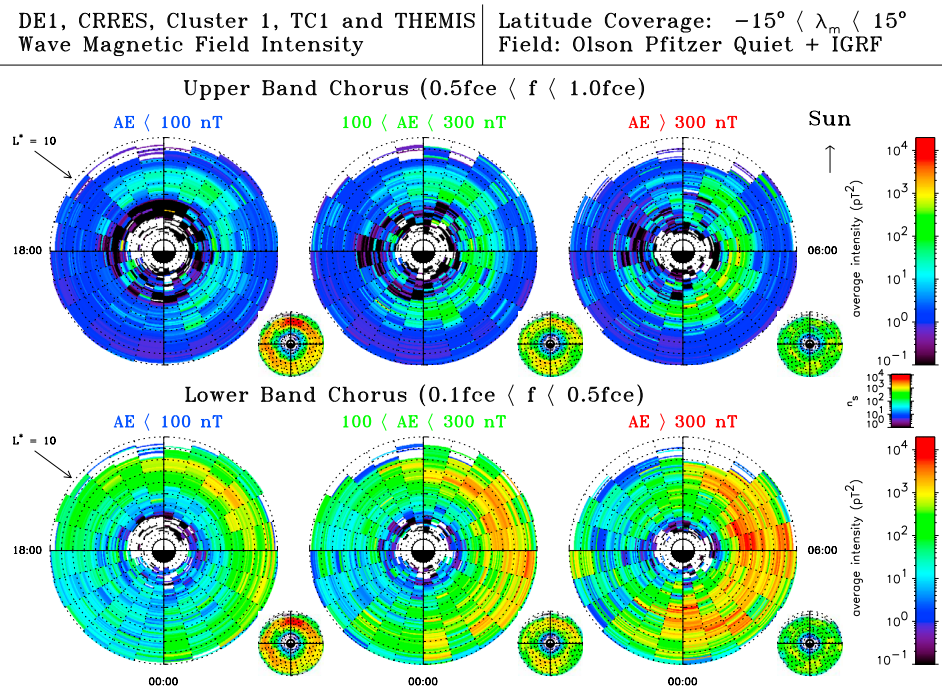


Figure 4. Combined satellite model of the equatorial wave intensity for (top) upper band chorus and (bottom) lower band chorus as a function of L^* , MLT and geomagnetic activity. The average intensities are shown in the large panels and the corresponding sampling distributions in the small panels.

1100 MLT, but are largest, up to several hundred pT^2 from $4 < L^* < 6$ from 0000 to 0600 MLT.

[40] These results confirm that lower and upper band chorus are largely substorm dependent with the largest intensities being seen during active conditions. The local time dependence of these intensity enhancements is generally consistent with electron injection from substorms near midnight and subsequent drift around dawn to the dayside.

7.1.2. Midlatitude Region ($15^\circ < |\lambda_m| < 30^\circ$)

[41] The average midlatitude ($15^\circ < |\lambda_m| < 30^\circ$) lower band chorus intensities are shown as a function of L^* , MLT and geomagnetic activity in Figure 5 (bottom). The midlatitude lower band chorus is also largely substorm-dependent with peak intensities of the order of $2000 pT^2$ during active conditions. However, the spatial dependence is different from the equatorial lower band chorus with the largest intensities being restricted to the region $4 < L^* < 9$, primarily from 0700 to 1400 MLT.

[42] The average midlatitude upper band chorus intensities are shown in the same format in Figure 5 (top). In sharp contrast, midlatitude upper band chorus is extremely weak, even during active conditions, with intensities typically less than $1 pT^2$.

7.2. Latitudinal Distribution

7.2.1. Evening to Dawn Sector (2100–0600 MLT)

[43] The average lower and upper band chorus wave intensities for the evening to dawn sector (2100–0600 MLT) are shown as a function of the radial distance from the center of the Earth projected onto the plane of the magnetic equator, r , Solar Magnetospheric (SM) z and geomagnetic activity in Figure 6. Dipole field lines and lines of constant magnetic latitude are included to help visualize the behavior

of the wave intensities as a function of L^* and λ_m . As before the average intensities are plotted in the large panels and the corresponding sampling distributions in the small panels. Upper band chorus (Figure 6, top) occurs predominantly in the region $3 < L^* < 7$ and is tightly confined to the equatorial plane, lying largely within 6° of the magnetic equator. Lower band chorus covers a larger region of geospace, extending from $4 < L^* < 10$. The largest lower band chorus intensities in this region are seen during active conditions and are confined to within about 12° of the magnetic equator.

7.2.2. Dawn to Afternoon Sector (0600–1500 MLT)

[44] The average lower and upper band chorus wave intensities for the dawn to afternoon sector (0600–1500 MLT) are shown in Figure 7. The upper band chorus remains confined within 6° of the magnetic equator. In contrast, the lower band chorus is substorm dependent and extends to higher latitudes, up to about 30° in this sector. Beyond 30° there is little lower band chorus wave power.

8. Discussion

[45] Our global statistical model of whistler mode chorus combines information from five satellites, extending the coverage and improving the statistics of existing models. An important difference between this model and preceding models based on CRRES data [Meredith *et al.*, 2001, 2003] is the use of L^* rather than McIlwain L so that the wave models can be directly incorporated into radiation belt models. From the plasmopause out to $L^* = 10$ the chorus emissions are found to be largely substorm dependent with the largest intensities being seen during active conditions. The global morphology of the chorus emissions is broadly consistent with previous observations of chorus occurrence

DE1, CRRES, Cluster 1, TC1 and THEMIS Wave Magnetic Field Intensity	Latitude Coverage: $15^\circ < \lambda_m < 30^\circ$ Field: Olson Pfitzer Quiet + IGRF
--	---

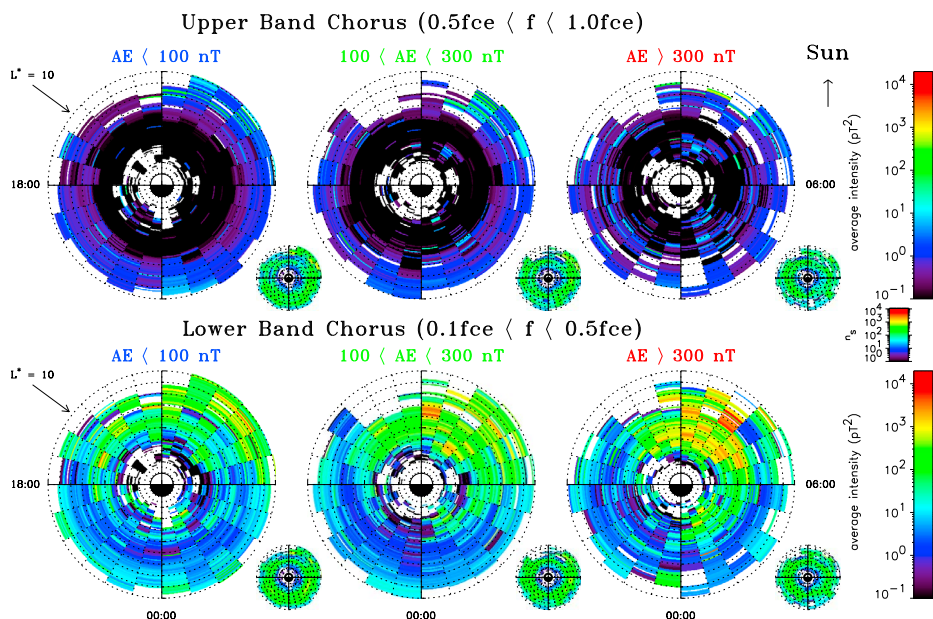


Figure 5. Combined satellite model of the midlatitude wave intensity for (top) upper band chorus and (bottom) lower band chorus as a function of L^* , MLT and geomagnetic activity. The average intensities are shown in the large panels and the corresponding sampling distributions in the small panels.

DE1, CRRES, Cluster 1, TC1 and THEMIS Wave Magnetic Field Intensity	MLT Coverage: 21–06 MLT Field: Olson Pfitzer Quiet + IGRF
--	--

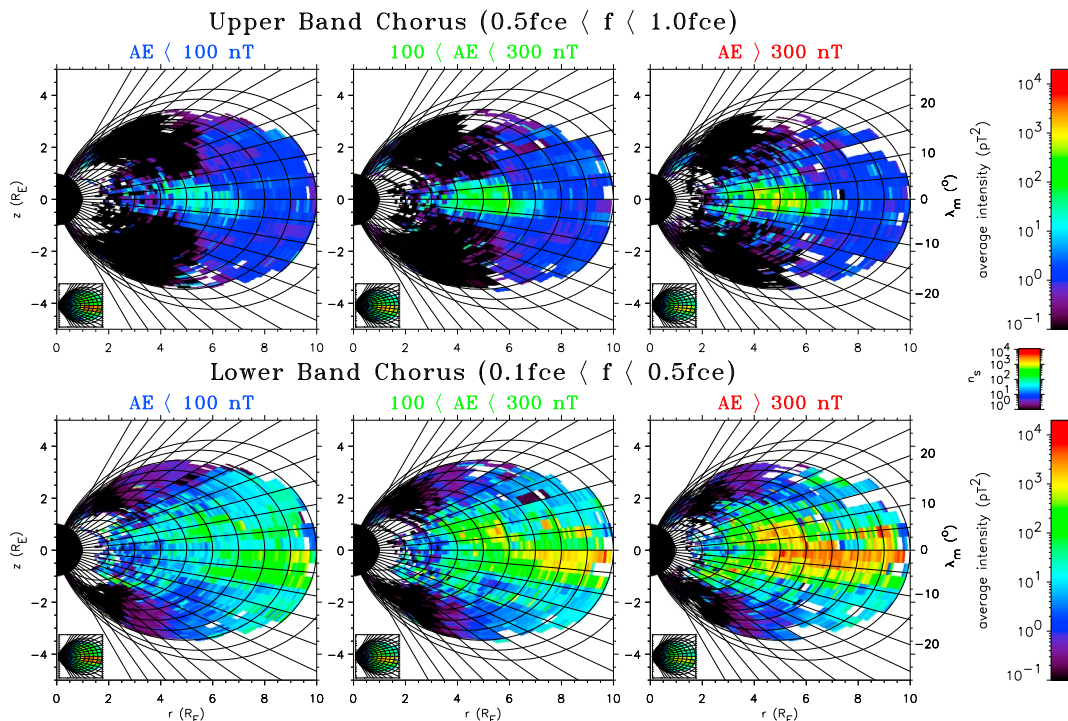


Figure 6. Combined satellite model of the distribution of the wave intensity for (top) upper band chorus and (bottom) lower band chorus as a function of radial distance from the center of the Earth projected onto the plane of the magnetic equator, r , and SM z and geomagnetic activity for the 2100–0600 MLT sector. The average intensities are shown in the large panels and the corresponding sampling distributions in the small panels.

DE1, CRRES, Cluster 1, TC1 and THEMIS | MLT Coverage: 06–15 MLT
 Wave Magnetic Field Intensity | Field: Olson Pfitzer Quiet + IGRF

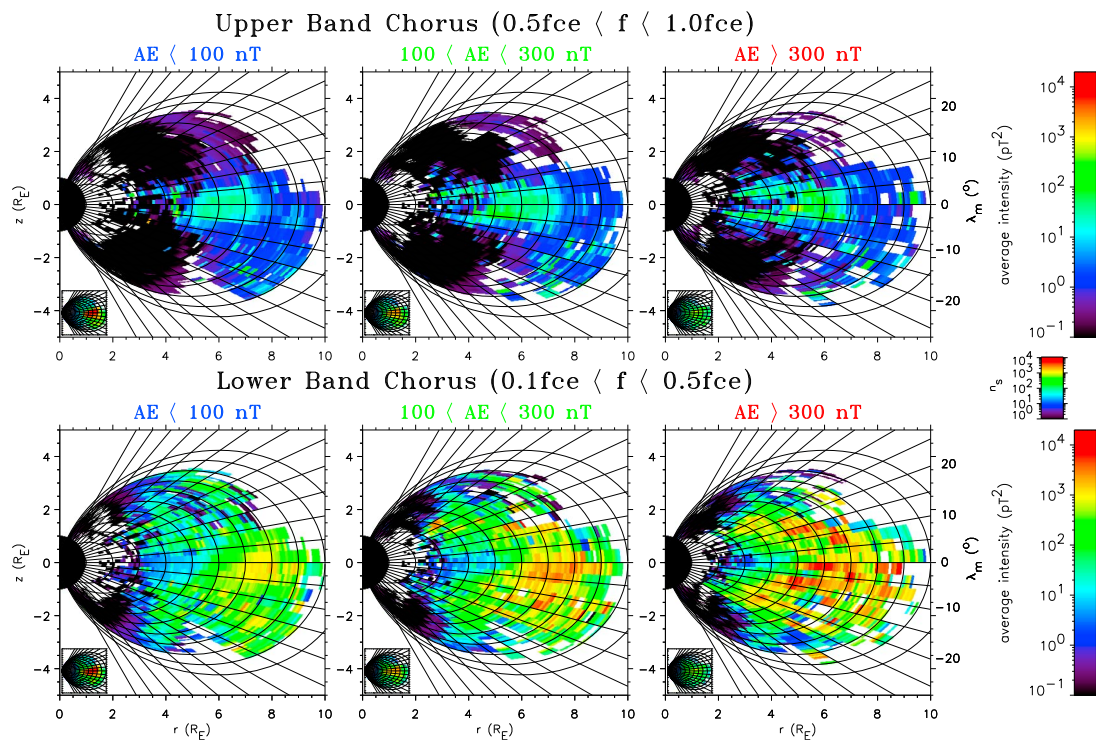


Figure 7. Combined satellite model of the distribution of the wave intensity for (top) upper band chorus and (bottom) lower band chorus as a function of radial distance from the center of the Earth projected onto the plane of the magnetic equator, r , SM z and geomagnetic activity for the 0600–1500 MLT sector. The average intensities are shown in the large panels and the corresponding sampling distributions in the small panels.

statistics with equatorial emissions being observed primarily on the dawn-side [Tsurutani and Smith, 1977; Koons and Roeder, 1990] while emissions at higher latitudes are largely confined to the dayside [Tsurutani and Smith, 1977].

[46] The global model of lower band chorus magnetic field intensities that has been used in several recent radiation belt models [Varotsou et al., 2005, 2008; Fok et al., 2008; Albert et al., 2009] was derived from CRRES electric field data using the cold plasma dispersion relation and assuming parallel propagation. Observations suggest that this may be a reasonable assumption since the wave normal angles of lower band chorus in the equatorial region are predominantly small and less than 20° [Li et al., 2011]. Indeed, comparison of the equatorial lower band chorus intensities in the region of overlap with Double Star TC1 and THEMIS show good general agreement with intensities of the order of 2000 pT^2 during active conditions in the region $4 < L^* < 6$ from 2300 to 0800 MLT.

[47] During active conditions enhanced lower band chorus is observed primarily on the dawnside from the plasmopause out to $L^* = 9$. Lower band chorus can thus cause acceleration and loss of electrons over a wide range of geospace. Current radiation belt models driven by chorus wave data from CRRES extend out to geosynchronous orbit in the magnetic equatorial plane which roughly corresponds to $L^* = 6$. The next generation of radiation belt models should include the effects of lower band chorus at larger values of L^* out to

the outer boundary of the model. Nevertheless, the most favorable conditions for acceleration to relativistic energies are likely to remain near the plasmopause where f_{pe}/f_{ce} is low [Li et al., 2010b].

[48] On the nightside lower band chorus is confined to magnetic latitudes less than 15° due to strong Landau damping by suprathermal electrons [Bortnik et al., 2007]. On the dayside the flux of suprathermal electrons is much weaker [Meredith et al., 2004; Li et al., 2010a] and lower band chorus is observed at higher latitudes, up to $\pm 30^\circ$. Chorus wave power is observed at even higher latitudes on the dayside [e.g., Bunch et al., 2011, 2012] but, at these higher latitudes, the frequency of the waves typically falls below 0.1 times the local gyrofrequency and is consequently outside the range of lower band chorus as defined in this paper. In contrast, upper band chorus is largely confined to within about 6° of the magnetic equator at all local times due to stronger Landau damping at higher frequencies [Bortnik et al., 2007].

[49] Upper band and lower band chorus both contribute to the diffuse aurora, with upper band and lower band chorus typically interacting with electrons with energies less than and greater than a few keV respectively [e.g. Thorne et al., 2010]. Our results show that there is little or no upper band chorus wave activity beyond $L^* = 7$, consistent with previous studies [Santolik et al., 2005; Li et al., 2011]. At higher values of L^* upper band chorus cannot be responsible

for the diffuse auroral electron precipitation at energies less than a few keV. Electron cyclotron harmonic (ECH) waves, which can also resonate with electrons with energies less than a few keV, extend beyond $L^* = 7$ out to 10–12 R_E [Roeder and Koons, 1989; Ni et al., 2011b]. ECH waves, which do not play a significant role in the formation of the diffuse aurora at low L^* [Thorne et al., 2010], may thus ultimately play an important role at higher values of L^* . Indeed, a recent case study involving conjugate ground and space measurements suggests that ECH waves can be the dominant driver of the diffuse aurora in the outer magnetosphere [Liang et al., 2011; Ni et al., 2012].

[50] This study does not take into account the very large amplitude ($E_w > 100$ mV/m) whistler mode chorus waves which have been observed recently by several spacecraft [e.g., Cattell et al., 2008; Cully et al., 2008b]. These waves typically last for a few tenths of a second and do not appear as very large amplitudes in the time averages of the wave data used in this study. These very large amplitude waves lead to pronounced non-linear effects and, as such, may also be very effective for acceleration [e.g., Omura et al., 2007; Cattell et al., 2008; Bortnik et al., 2008b; Tao et al., 2012] and loss [Kersten et al., 2011] of relativistic electrons, depending on how often they occur. The relative roles of non-linear versus quasi-linear interactions with whistler mode chorus remain an important and challenging question in radiation belt physics, and one that will be addressed by ongoing studies and future missions such as the US Radiation Belt Storm Probes and the Japanese ERG satellite.

9. Conclusions

[51] We have developed a new global model of whistler mode chorus using data from five satellites to extend the coverage and improve the statistics of existing models developed from single satellites. Our main conclusions are as follows.

[52] 1. From the plasmopause out to $L^* = 10$ the chorus emissions are found to be largely substorm dependent with the largest intensities being seen during active conditions.

[53] 2. Equatorial lower band chorus is strongest during active conditions with peak intensities of the order 2000 pT^2 in the region $4 < L^* < 9$ between 2300 and 1200 MLT.

[54] 3. Equatorial upper band chorus is both weaker and less extensive with peak intensities of the order a few hundred pT^2 between 2300 and 1100 MLT but only extending from $L^* = 3$ to $L^* = 7$.

[55] 4. Midlatitude lower band chorus is strongest in the lower band during active conditions with peak intensities of the order 2000 pT^2 in the region $4 < L^* < 9$ but only on the dayside between 0700 and 1400 MLT.

[56] 5. Midlatitude upper band chorus is extremely weak, even during active conditions, with intensities less than 1 pT^2 .

[57] Our model of whistler mode chorus will be used to compute pitch angle and energy diffusion coefficients from the plasmopause out to $L^* = 10$. The new diffusion coefficients will be incorporated into the BAS and ONERA global radiation belt models to improve the modeling and forecasting of the radiation belt environment.

[58] **Acknowledgments.** We acknowledge Roger Anderson for provision of the CRRES plasma wave data. We also acknowledge the CDAWeb and CLUSTER Active Archive Web sites for the provision of the wave data of DE1 and CLUSTER, respectively. We thank LPCEE laboratory (Orléans, France) for their help in the analysis of the wave data. We thank NASA contract NAS5-02099 and V. Angelopoulos for use of data from THEMIS Mission. Specifically, we thank O. Le Contel and A. Roux for use of SCM data; J. W. Bonnell and F. S. Mozer for use of EFI data; and K. H. Glassmeier, U. Auster, and W. Baumjohann for the use of FGM data provided under the lead of the Technical University of Braunschweig and with financial support through the German Ministry for Economy and Technology and the German Center for Aviation and Space (DLR) under contract 50 OC 0302. We also thank the NSSDC Omniweb for the provision of the geomagnetic activity indices used in this report. R.M.T. and W.L. would like to acknowledge support from NASA grants NNX11AR64G and NNX11AD75G. The research leading to these results has received funding from the European Union Seventh Framework Programme (FP7/2007-2013) under grant agreement 262468 and the Natural Environment Research Council.

[59] Robert Lysak thanks the reviewers for their assistance in evaluating this paper.

References

- Albert, J. M., N. P. Meredith, and R. B. Horne (2009), Three-dimensional diffusion simulation of outer radiation belt electrons during the October 9, 1990, magnetic storm, *J. Geophys. Res.*, *114*, A09214, doi:10.1029/2009JA014336.
- Anderson, R. R., D. A. Gurnett, and D. L. Odem (1992), CRRES plasma wave experiment, *J. Spacecr. Rockets*, *29*, 570–573.
- Angelopoulos, V. (2008), The THEMIS Mission, *Space Sci. Rev.*, *141*(1–4), 5–34, doi:10.1007/s11214-008-9336-1.
- Auster, H. U., et al. (2008), The THEMIS fluxgate magnetometer, *Space Sci. Rev.*, *141*, 235–264, doi:10.1007/s11214-008-9365-9.
- Baker, D. N., J. B. Blake, L. B. Callis, J. R. Cummings, D. Hovestadt, S. Kanekal, B. Klecker, R. A. Mewaldt, and R. D. Zwickl (1994), Relativistic electron acceleration and decay time scales in the inner and outer radiation belts: SAMPEX, *Geophys. Res. Lett.* *21*(6), 409–412, doi:10.1029/93GL03532.
- Balogh, A., et al. (2001), The Cluster Magnetic Field Investigation: Overview of in-flight performance and initial results, *Ann. Geophys.*, *19*, 1207–1217, doi:10.5194/angeo-19-1207-2001.
- Blake, J. B., W. A. Kolasinski, R. W. Fillius, and E. G. Mullen (1992), Injection of electrons and protons with energies of tens of MeV into $L < 3$ on 24 March 1991, *Geophys. Res. Lett.*, *19*(8), 821–824.
- Bortnik, J., and R. M. Thorne (2007), The dual role of ELF/VLF chorus waves in the acceleration and precipitation of radiation belt electrons, *J. Atmos. Sol. Terr. Phys.*, *69*, 378–386, doi:10.1016/j.jastp.2006.05.030.
- Bortnik, J., R. M. Thorne, and N. P. Meredith (2007), Modeling the propagation characteristics of chorus using CRRES suprathermal electron fluxes, *J. Geophys. Res.*, *112*, A08204, doi:10.1029/2006JA012237.
- Bortnik, J., R. M. Thorne, and N. P. Meredith (2008a), The unexpected origin of plasmaspheric hiss from discrete chorus emissions, *Nature*, *452*, 62–66, doi:10.1038/nature06741.
- Bortnik, J., R. M. Thorne, and U. S. Inan (2008b), Nonlinear interaction of energetic electrons with large amplitude chorus, *Geophys. Res. Lett.*, *35*, L21102, doi:10.1029/2008GL035500.
- Bortnik, J., W. Li, R. M. Thorne, V. Angelopoulos, C. Cully, J. Bonnell, O. Le Contel, and A. Roux (2009), An observation linking the origin of plasmaspheric hiss to discrete chorus emissions, *Science*, *324*(5928), 775–778, doi:10.1126/science.1171273.
- Bortnik, J., L. Chen, W. Li, N. P. Meredith, and R. B. Horne (2011), Modelling the wave power distribution and characteristics of plasmaspheric hiss, *J. Geophys. Res.*, *116*, A12209, doi:10.1029/2011JA016862.
- Bunch, N. L., M. Spasojevic, and Y. Y. Shprits (2011), On the latitudinal extent of chorus emissions as observed by the Polar Plasma Wave Instrument, *J. Geophys. Res.*, *116*, A04204, doi:10.1029/2010JA016181.
- Bunch, N. L., M. Spasojevic, and Y. Y. Shprits (2012), Off-equatorial chorus occurrence and wave amplitude distributions as observed by the Polar Plasma Wave Instrument, *J. Geophys. Res.*, *117*, A04205, doi:10.1029/2011JA017228.
- Burtis, W. J., and R. A. Helliwell (1976), Magnetospheric chorus: Occurrence patterns and normalized frequency, *Planet Space Sci.*, *24*, 1007–1024.
- Carpenter, D. L., and R. R. Anderson (1992), An ISEE/whistler model of equatorial electron density in the magnetosphere, *J. Geophys. Res.*, *97*, 1097–1108, doi:10.1029/91JA01548.
- Carpenter, D. L., F. Walter, R. E. Barrington, and D. J. McEwen (1968), Alouette 1 and 2 observations of abrupt changes in whistler rate and of

- VLF noise variations at the plasmopause?: A satellite-ground study, *J. Geophys. Res.*, *79*, 2929–2940, doi:10.1029/JA073i009p02929.
- Carpenter, D. L., C. G. Park, H. A. Taylor Jr., and H. C. Brinton (1969), Multi-experiment detection of the plasmopause from EOGO satellites and Antarctic ground stations, *J. Geophys. Res.*, *74*, 1837–1847, doi:10.1029/JA074i007p01837.
- Carr, C., et al. (2005), The Double Star magnetic field investigation: Instrument design, performance and highlights of the first year's observations, *Ann. Geophys.*, *23*, 2713–2732, doi:10.5194/angeo-23-2713-2005.
- Cattell, C., et al. (2008), Discovery of very large amplitude whistler-mode waves in Earth's radiation belts, *Geophys. Res. Lett.*, *35*, L01105, doi:10.1029/2007GL032009.
- Chan, K.-W., and R. E. Holzer (1976), ELF hiss associated with plasma density enhancements in the outer magnetosphere, *J. Geophys. Res.*, *81*, 2267–2274, doi:10.1029/JA081i013p02267.
- Chen, L., W. Li, J. Bortnik, and R. M. Thorne (2012a), Amplification of whistler-mode hiss inside the plasmasphere, *Geophys. Res. Lett.*, *39*, L08111, doi:10.1029/2012GL051488.
- Chen, L., J. Bortnik, W. Li, R. M. Thorne, and R. B. Horne (2012b), Modeling the properties of plasmaspheric hiss: 1. Dependence on chorus wave emission, *J. Geophys. Res.*, *117*, A05201, doi:10.1029/2011JA017201.
- Chen, L., J. Bortnik, W. Li, R. M. Thorne, and R. B. Horne (2012c), Modeling the properties of plasmaspheric hiss: 2. Dependence on the plasma density distribution, *J. Geophys. Res.*, *117*, A05202, doi:10.1029/2011JA017202.
- Cornilleau-Wehrin, N., R. Gendrin, F. Lefeuvre, M. Parrot, R. Grard, D. Jones, A. Bahnsen, E. Ungstrup, and W. Gibbons (1978), VLF electromagnetic waves observed onboard GEOS-1, *Space Sci. Rev.*, *22*, 371–382.
- Cornilleau-Wehrin, N., et al. (1997) The CLUSTER Spatio-Temporal Analysis of Field Fluctuations (STAFF) Experiment, *Space Sci. Rev.*, *79*, 107–136.
- Cornilleau-Wehrin, N., et al. (2003), First results obtained by the Cluster STAFF experiment, *Ann. Geophys.*, *21*, 437–456.
- Cornilleau-Wehrin, N., et al. (2005), The STAFF-DWP wave instrument on the DSP equatorial spacecraft: Description and first results, *Ann. Geophys.*, *23*, 2785–2801.
- Cully, C. M., R. E. Ergun, K. Stevens, A. Nammari, and J. Westfall (2008a), The THEMIS digital fields board, *Space Sci. Rev.*, *141* (1–4), 343–355, doi:10.1007/s11214-008-9417-1.
- Cully, C. M., J. W. Bonnell, and R. E. Ergun (2008b), THEMIS observations of long-lived regions of large-amplitude whistler waves in the inner magnetosphere, *Geophys. Res. Lett.*, *35*, L17S16, doi:10.1029/2008GL033643.
- Décéau, P. M. E., et al. (1993), WHISPER, a sounder and high-frequency wave analyser experiment, *Eur. Space Agency Spec. Publ.*, *1159*, 51–67.
- Décéau, P. M. E., et al. (1997), WHISPER, a resonance sounder and wave analyser: Performances and perspectives for the CLUSTER mission, *Space Sci. Rev.*, *79*, 157–193.
- Dunckel, N., and R. A. Helliwell (1969), Whistler-Mode Emissions on the OGO 1 Satellite, *J. Geophys. Res.*, *74*, 6371–6385, doi:10.1029/JA074i026p06371.
- Farthing, W. H., M. Sugiura, B. G. Ledley, and L. J. Cahill Jr. (1981), Magnetic field observations on DE-A and -B, *Space Science Instr.*, *5*, 551–560.
- Fok, M.-C., R. B. Horne, N. P. Meredith, and S. A. Glauert (2008), Radiation Belt Environment Model: Application to space weather nowcasting, *J. Geophys. Res.*, *113*, A03S08, doi:10.1029/2007JA012558.
- Friedel, R. H. W., S. Bourdaric, and T. E. Cayton (2005), Intercalibration of magnetospheric energetic electron data, *Space Weather*, *3*, S09B04, doi:10.1029/2005SW000153.
- Gurnett, D. A., and R. R. Shaw (1973), Electromagnetic radiation trapped in the magnetosphere above the plasma frequency, *J. Geophys. Res.*, *78*, 8136–8149, doi:10.1029/JA078i034p08136.
- Gustafsson, G., et al. (1997), The electric field and wave experiment for the Cluster mission, *Space Sci. Rev.*, *79*, 137–156.
- Horne, R. B. (2002), The contribution of wave-particle interactions to electron loss and acceleration in the Earth's radiation belts during geomagnetic storms, in *URSI Review of Radio Science 1999–2002*, edited by W. R. Stone, pp. 801–828, John Wiley, New York.
- Horne, R. B., R. M. Thorne, S. A. Glauert, J. M. Albert, N. P. Meredith, and R. R. Anderson (2005), Timescale for radiation belt electron acceleration by whistler mode chorus waves, *J. Geophys. Res.*, *110*, A03225, doi:10.1029/2004JA010811.
- Horne, R. B., N. P. Meredith, S. A. Glauert, A. Varotsou, D. Boscher, R. M. Thorne, Y. Y. Shprits, and R. R. Anderson (2006), Mechanisms for the acceleration of radiation belt electrons, in *Recurrent Magnetic Storms: Corotating Solar Wind Streams*, *Geophys. Monogr. Ser.*, vol. 167, edited by B. Tsurutani et al., pp. 151–173, AGU, Washington, D. C., doi:10.1029/167GM14.
- Katoh, Y., and Y. Omura (2007), Computer simulation of chorus wave generation in the Earth's inner magnetosphere, *Geophys. Res. Lett.*, *34*, L03102, doi:10.1029/2006GL028594.
- Kersten, K., C. A. Cattell, A. Breneman, K. Goetz, P. J. Kellogg, J. R. Wygant, L. B. Wilson III, J. B. Blake, M. D. Looper, and I. Roth (2011), Observation of relativistic electron microbursts in conjunction with intense radiation belt whistler-mode waves, *Geophys. Res. Lett.*, *38*, L08107, doi:10.1029/2011GL046810.
- Koons, H. C., and J. L. Roeder (1990), A survey of equatorial magnetospheric wave activity between 5 and 8 RE, *Planet. Space Sci.*, *38*, 1335–1341.
- Lam, M. M., R. B. Horne, N. P. Meredith, and S. A. Glauert (2007), Modeling the effects of radial diffusion and plasmaspheric hiss on outer radiation belt electrons, *Geophys. Res. Lett.*, *34*, L20112, doi:10.1029/2007GL031598.
- Lauben, D. S., U. S. Inan, T. F. Bell, and D. A. Gurnett (2002), Source characteristics of ELF/VLF chorus, *J. Geophys. Res.*, *107*(A12), 1429, doi:10.1029/2000JA003019.
- Le Contel, O., et al. (2008), First results of the THEMIS search coil magnetometers, *Space Sci. Rev.*, *141*(1–4), 509–534, doi:10.1007/s11214-008-9371-y.
- LeDocq, M. J., D. A. Gurnett, and G. B. Hospodarsky (1998), Chorus source locations from VLF Poynting flux measurements with the Polar spacecraft, *Geophys. Res. Lett.*, *25*(21), 4063–4066, doi:10.1029/1998GL900071.
- Li, W., R. M. Thorne, N. P. Meredith, R. B. Horne, J. Bortnik, Y. Y. Shprits, and B. Ni (2008), Evaluation of whistler mode chorus amplification during an injection event observed on CRRES, *J. Geophys. Res.*, *113*, A09210, doi:10.1029/2008JA013129.
- Li, W., R. M. Thorne, V. Angelopoulos, J. W. Bonnell, J. P. McFadden, C. W. Carlson, O. LeContel, A. Roux, K. H. Glassmeier, and H. U. Auster (2009a), Evaluation of whistler-mode chorus intensification on the nightside during an injection event observed on the THEMIS spacecraft, *J. Geophys. Res.*, *114*, A00C14, doi:10.1029/2008JA013554.
- Li, W., R. M. Thorne, V. Angelopoulos, J. Bortnik, C. M. Cully, B. Ni, O. LeContel, A. Roux, U. Auster, and W. Magnes (2009b), Global distribution of whistler-mode chorus waves observed on the THEMIS spacecraft, *Geophys. Res. Lett.*, *36*, L09104, doi:10.1029/2009GL037595.
- Li, W., R. M. Thorne, J. Bortnik, Y. Nishimura, V. Angelopoulos, L. Chen, J. P. McFadden, and J. W. Bonnell (2010a), Global distributions of suprathermal electrons observed on THEMIS and potential mechanisms for access into the plasmasphere, *J. Geophys. Res.*, *115*, A00J10, doi:10.1029/2010JA015687.
- Li, W., et al. (2010b), THEMIS analysis of observed equatorial electron distributions responsible for the chorus excitation, *J. Geophys. Res.*, *115*, A00F11, doi:10.1029/2009JA014845.
- Li, W., J. Bortnik, R. M. Thorne, and V. Angelopoulos (2011), Global distribution of wave amplitudes and wave normal angles of chorus waves using THEMIS wave observations, *J. Geophys. Res.*, *116*, A12205, doi:10.1029/2011JA017035.
- Liang, J., B. Ni, E. Spanswick, M. Kubyskhina, E. F. Donovan, V. M. Uritsky, R. M. Thorne, and V. Angelopoulos (2011), Fast earthward flows, electron cyclotron harmonic waves, and diffuse auroras: Conjunctive observations and a synthesized scenario, *J. Geophys. Res.*, *116*, A12220, doi:10.1029/2011JA017094.
- Lorentzen, K. R., J. B. Blake, U. S. Inan, and J. Bortnik (2001), Observations of relativistic electron microbursts in association with VLF chorus, *J. Geophys. Res.*, *106*, 6017–6027, doi:10.1029/2000JA003018.
- Lyons, L. R., and R. M. Thorne (1973), Equilibrium structure of radiation belt electrons, *J. Geophys. Res.*, *78*(13), 2142–2149, doi:10.1029/JA078i013p02142.
- McCullough, J. P., J. L. Gannon, D. N. Baker, and M. Gehmeyr (2008), A statistical comparison of commonly used external magnetic field models, *Space Weather*, *6*, S10001, doi:10.1029/2008SW000391.
- Meredith, N. P., R. B. Horne, and R. R. Anderson (2001), Substorm dependence of chorus amplitudes: implications for the acceleration of electrons to relativistic energies, *J. Geophys. Res.*, *106*, 13,165–13,178.
- Meredith, N. P., R. B. Horne, D. Summers, R. M. Thorne, R. H. A. Iles, D. Heynderickx and R. R. Anderson (2002), Evidence for acceleration of outer zone electrons to relativistic energies by whistler mode chorus, *Ann. Geophys.*, *20*, 967–979.
- Meredith, N. P., R. B. Horne, R. M. Thorne, and R. R. Anderson (2003), Favored regions for chorus-driven electron acceleration to relativistic energies in the Earth's outer radiation belt, *Geophys. Res. Lett.*, *30*(16), 1871, doi:10.1029/2003GL017698.
- Meredith, N. P., R. B. Horne, R. M. Thorne, D. Summers, and R. R. Anderson (2004), Substorm dependence of plasmaspheric hiss, *J. Geophys. Res.*, *109*, A06209, doi:10.1029/2004JA010387.

- Meredith, N. P., R. B. Horne, S. A. Glauert, R. M. Thorne, D. Summers, J. M. Albert, and R. R. Anderson (2006a), Energetic outer zone electron loss timescales during low geomagnetic activity, *J. Geophys. Res.*, *111*, A05212, doi:10.1029/2005JA011516.
- Meredith, N. P., R. B. Horne, M. A. Clilverd, D. Horsfall, R. M. Thorne, and R. R. Anderson (2006b), Origins of plasmaspheric hiss, *J. Geophys. Res.*, *111*, A09217, doi:10.1029/2006JA011707.
- Meredith, N. P., R. B. Horne, S. A. Glauert, and R. R. Anderson (2007), Slot region electron loss timescales due to plasmaspheric hiss and lightning generated whistlers, *J. Geophys. Res.*, *112*, A08214, doi:10.1029/2007JA012413.
- Meredith, N. P., R. B. Horne, S. A. Glauert, D. N. Baker, S. G. Kanekal, and J. M. Albert (2009), Relativistic electron loss timescales in the slot region, *J. Geophys. Res.*, *114*, A03222, doi:10.1029/2008JA013889.
- Ni, B., R. M. Thorne, N. P. Meredith, R. B. Horne, and Y. Y. Shprits (2011a), Resonant scattering of plasma sheet electrons leading to diffuse auroral precipitation: 2. Evaluation for whistler mode chorus waves, *J. Geophys. Res.*, *116*, A04219, doi:10.1029/2010JA016233.
- Ni, B., R. Thorne, J. Liang, V. Angelopoulos, C. Cully, W. Li, X. Zhang, M. Hartinger, O. Le Contel, and A. Roux (2011b), Global distribution of electrostatic electron cyclotron harmonic waves observed on THEMIS, *Geophys. Res. Lett.*, *38*, L17105, doi:10.1029/2011GL048793.
- Ni, B., J. Liang, R. M. Thorne, V. Angelopoulos, R. B. Horne, M. Kubyskhina, E. Spanswick, E. F. Donovan, and D. Lummerzheim (2012), Efficient diffuse auroral electron scattering by electrostatic electron cyclotron harmonic waves in the outer magnetosphere: A detailed case study, *J. Geophys. Res.*, *117*, A01218, doi:10.1029/2011JA017095.
- Nishimura, Y., et al. (2010) Identifying the driver of the pulsating aurora, *Science*, *330*, 81–84, doi:10.1126/science.1193186.
- Olson, W. P., and K. Pfizter (1977), Magnetospheric magnetic field modelling annual scientific report, report, Air Force Off. of Sci. Res., Arlington, Va.
- O'Brien, T. P., M. D. Looper, and J. B. Blake (2004), Quantification of relativistic electron microburst losses during the GEM storms, *Geophys. Res. Lett.*, *31*, L04802, doi:10.1029/2003GL018621.
- Omura, Y., N. Furuya, and D. Summers (2007), Relativistic turning acceleration of resonant electrons by coherent whistler mode waves in a dipole magnetic field, *J. Geophys. Res.*, *112*, A06236, doi:10.1029/2006JA012243.
- Omura, Y., Y. Katoh, and D. Summers (2008), Theory and simulation of the generation of whistler-mode chorus, *J. Geophys. Res.*, *113*, A04223, doi:10.1029/2007JA012622.
- Parrot, M., and F. Lefeuvre (1986), Statistical study of the propagation characteristics of ELF hiss observed on GEOS 1, inside and outside the plasmasphere, *Ann. Geophys.*, *4*, 363–384.
- Platino, M., U. S. Inan, T. F. Bell, D. A. Gurnett, J. S. Pickett, P. Canu, and P. M. E. Décréau (2005), Whistlers observed by the Cluster spacecraft outside the plasmasphere, *J. Geophys. Res.*, *110*, A03212, doi:10.1029/2004JA010730.
- Reeves, G. D., K. L. McAdams, R. H. W. Friedel, and T. P. O'Brien (2003), Acceleration and loss of relativistic electrons during geomagnetic storms, *Geophys. Res. Lett.*, *30*(10), 1529, doi:10.1029/2002GL016513.
- Roeder, J. L., and H. C. Koons (1989), A survey of electron cyclotron waves in the magnetosphere and the diffuse auroral electron precipitation, *J. Geophys. Res.*, *94*(A3), 2529–2541, doi:10.1029/JA094iA03p02529.
- Roux, A., O. Le Contel, C. Coillot, A. Bouabdellah, B. de la Porte, D. Alison, S. Ruocco, and M. C. Vassal (2008), The search coil magnetometer for THEMIS, *Space Sci. Rev.*, *141*(1–4), 265–275, doi:10.1007/s11214-008-9455-8.
- Russell, C. T., R. E. Holzer, and E. J. Smith (1969), OGO 3 observations of ELF noise in the magnetosphere, 1. Spatial extent and frequency of occurrence, *J. Geophys. Res.*, *74*, 755–777, doi:10.1029/JA074i003p00755.
- Santolík, O., D. A. Gurnett, J. S. Pickett, M. Parrot, and N. Cornilleau-Wehrin (2004), A microscopic and nanoscopic view of storm-time chorus on 31 March 2001, *Geophys. Res. Lett.*, *31*, L02801, doi:10.1029/2003GL018757.
- Santolík, O., D. A. Gurnett, J. S. Pickett, M. Parrot and N. Cornilleau-Wehrin (2005), Central position of the source region of storm time chorus, *Planet. Space Sci.*, *53*, 299–305.
- Shawhan, S. D., D. A. Gurnett, D. L. Odem, R. A. Helliwell, and C. G. Park (1981), The plasma wave and quasi-static electric field instrument (PWI) for Dynamics Explorer-A, *Space Sci. Instrumen.*, *5*, 535–550.
- Shue, J.-H., et al. (1998), Magnetopause location under extreme solar wind conditions, *J. Geophys. Res.*, *103*(A8), 17,691–17,700, doi:10.1029/98JA01103.
- Singer, H. J., W. P. Sullivan, P. Anderson, F. Mozer, P. Harvey, J. Wygant, and W. McNeil (1992), Fluxgate magnetometer instrument on the CRRES, *J. Spacecr. Rockets*, *29*, 599–601.
- Subbotin, D., Y. Shprits, and B. Ni (2010), Three-dimensional VERB radiation belt simulations including mixed diffusion, *J. Geophys. Res.*, *115*, A03205, doi:10.1029/2009JA015070.
- Summers, D., B. Ni, and N. P. Meredith (2007), Timescales for radiation belt electron acceleration and loss due to resonant wave particle interactions: 2. Evaluation for VLF chorus, ELF hiss, and EMIC waves, *J. Geophys. Res.*, *112*, A04207, doi:10.1029/2006JA011993.
- Summers, D., B. Ni, N. P. Meredith, R. B. Horne, R. M. Thorne, M. B. Moldwin, and R. R. Anderson (2008), Electron scattering by whistler-mode (ELF) hiss in plasmaspheric plumes, *J. Geophys. Res.*, *113*, A04219, doi:10.1029/2007JA012678.
- Tao, X., J. Bortnik, R. M. Thorne, J. M. Albert, and W. Li (2012), Effects of amplitude modulation on nonlinear interactions between electrons and chorus waves, *Geophys. Res. Lett.*, *39*, L06102, doi:10.1029/2012GL051202.
- Thorne, R. M. (2010), Radiation belt dynamics: The importance of wave-particle interactions, *Geophys. Res. Lett.*, *37*, L22107, doi:10.1029/2010GL044990.
- Thorne, R. M., E. J. Smith, R. K. Burton, and R. E. Holzer (1973), Plasmaspheric hiss, *J. Geophys. Res.*, *78*, 1581–1596, doi:10.1029/JA078i010p01581.
- Thorne, R. M., R. B. Horne, S. Glauert, N. P. Meredith, Y. Y. Shprits, D. Summers, and R. R. Anderson (2005a), The influence of wave-particle interactions on relativistic electron dynamics during storms, in *Inner Magnetosphere Interactions: New Perspectives From Imaging*, *Geophys. Monogr. Ser.*, vol. 159, edited by J. Burch, M. Schulz, and H. Spence, pp. 101–112, AGU, Washington, D. C., doi:10.1029/159GM07.
- Thorne, R. M., T. P. O'Brien, Y. Y. Shprits, D. Summers, and R. B. Horne (2005b), Timescale for MeV electron microburst loss during geomagnetic storms, *J. Geophys. Res.*, *110*, A09202, doi:10.1029/2004JA010882.
- Thorne, R. M., B. Ni, X. Tao, R. B. Horne, and N. P. Meredith (2010), Scattering by chorus waves as the dominant cause of the Earth's diffuse aurora, *Nature*, *467*, 943–946, doi:10.1038/nature09467.
- Tsurutani, B. T., and E. J. Smith (1974), Postmidnight chorus: A substorm phenomenon, *J. Geophys. Res.*, *79*, 118–127.
- Tsurutani, B. T., and E. J. Smith (1977), Two types of magnetospheric ELF chorus and their substorm dependencies, *J. Geophys. Res.*, *82*, 5112–5128.
- Varotsou, A., D. Boscher, S. Bourdarie, R. B. Horne, S. A. Glauert, and N. P. Meredith (2005), Simulation of the outer radiation belt electrons near geosynchronous orbit including both radial diffusion and resonant interaction with Whistler-mode chorus waves, *Geophys. Res. Lett.*, *32*, L19106, doi:10.1029/2005GL023282.
- Varotsou, A., D. Boscher, S. Bourdarie, R. B. Horne, N. P. Meredith, S. A. Glauert, and R. H. Friedel (2008), Three-dimensional test simulations of the outer radiation belt electron dynamics including electron-chorus resonant interactions, *J. Geophys. Res.*, *113*, A12212, doi:10.1029/2007JA012862.
- Webb, F., and J. H. Allen (2004), Spacecraft and ground anomalies related to the October–November 2003 solar activity, *Space Weather*, *2*, S03008, doi:10.1029/2004SW000075.
- Wrenn, G. L. (1995), Conclusive evidence for internal dielectric charging anomalies on geosynchronous communications spacecraft, *J. Spacecr. Rockets*, *32*, 514–520.